Large refrigerant capacity in superparamagnetic iron nanoparticles embedded in a thin film matrix

Cite as: J. Appl. Phys. **132**, 193906 (2022); https://doi.org/10.1063/5.0120280
Submitted: 22 August 2022 • Accepted: 21 October 2022 • Published Online: 16 November 2022

Kaushik Sarkar, Surabhi Shaji, Suchit Sarin, et al.

Journal of Applied Physics ARTICLE scitation.org/journal/jap

Large refrigerant capacity in superparamagnetic iron nanoparticles embedded in a thin film matrix

Cite as: J. Appl. Phys. **132**, 193906 (2022); doi: 10.1063/5.0120280
Submitted: 22 August 2022 · Accepted: 21 October 2022 ·
Published Online: 16 November 2022

Kaushik Sarkar,[1] Surabhi Shaji,[1] Suchit Sarin,[2] Jeffrey E. Shield,[2,3] Christian Binek,[3,4] and Dhananjay Kumar[1,a)]

AFFILIATIONS

[1]Department of Mechanical Engineering, North Carolina A&T State University, Greensboro, North Carolina 27411, USA
[2]Mechanical and Materials Engineering, University of Nebraska-Lincoln, Lincoln, Nebraska 68588, USA
[3]Nebraska Center for Materials and Analysis, University of Nebraska-Lincoln, Lincoln, Nebraska 68588, USA
[4]Department of Physics and Astronomy, University of Nebraska-Lincoln, Lincoln, Nebraska 68588, USA

[a)]**Author to whom correspondence should be addressed:** dkumar@ncat.edu

ABSTRACT

A magnetocaloric effect (MCE) with sizable isothermal entropy change (ΔS) maintained over a broad range of temperatures above the blocking temperature is reported for a rare earth-free superparamagnetic nanoparticle system comprising of Fe–TiN heterostructure. Superparamagnetic iron (Fe) particles were embedded in a titanium nitride (TiN) thin film matrix in a TiN/Fe/TiN multilayered pattern using a pulsed laser deposition method. High angle annular dark-field images in conjunction with dispersive energy analysis, recorded using scanning transmission electron microscopy, show a clear presence of alternating layers of Fe and TiN with a distinct atomic number contrast between Fe particles and TiN. Quantitative information about the isothermal entropy change (ΔS) and the magnetocaloric effect in the multilayer Fe–TiN system has been obtained by applying Maxwell relation to the magnetization vs temperature data at various fields. With the absence of a dynamic magnetic hysteresis above the blocking temperature, the negative ΔS as high as 4.18×10^3 J/Km^3 (normal or forward MCE) is obtained at 3 T at 300 K.

I. INTRODUCTION

Magnetic refrigeration is a promising alternative in the modern-day quest for sustainable, energy-efficient, and environmentally friendly cooling technology. It is based on a physical phenomenon called the magnetocaloric effect (MCE).[1–4] The MCE describes the change of temperature (or entropy) of magnetic materials when it is subjected to an external magnetic field adiabatically (or isothermally) applied.[5] The MCE has shown immense potential for advanced cooling technologies since its first experimental observation in 1917 by Weiss and Piccard.[6] They observed the MCE in nickel near its Curie temperature of 627 K. They measured a temperature change of 0.7 K for an applied field of 1.5 T.[7] Later, Debye and Giauque explained the practical applications of MCE where ultra-low temperatures (<1 K) can be achieved by adiabatic demagnetization of paramagnetic salts.[8] The constant entropy condition associated with the adiabatic equilibrium process ensures that a field-induced reduction of the entropy of the spin degrees of freedom is compensated by an increase in the entropy of the lattice degrees of freedom, giving rise to an adiabatic temperature increase.[9] There has been a lot of research targeted to find suitable materials that have a sizeable MCE near room temperature in order to replace current compression/expansion cycle-based refrigerators which use harmful chlorofluorocarbons and hydrochlorofluorocarbons.[10] Materials that have been investigated include metallic materials,[11] intermetallic compounds,[12] melt-spun ribbons,[13,14] materials in a Laves phase,[15] manganites,[16] and Heusler alloys.[17] Nanoparticles and heterostructured systems can be used as an alternative to traditional bulk magnetocaloric materials (MCMs) due to control over the entropy change across the magnetic phase transition that can be maneuvered by varying particle size.[18,19] Exchange coupling between particles or clusters, intraplanar and interplanar exchange

interactions, interfacial strain, and magnetic anisotropy are reported to control the MCE of thin films and heterostructures.[20–23] In nanostructured materials, the isothermal entropy change (ΔS) can spread over a large range of temperatures that can drastically increase refrigerant capacity.[24,25]

Most of the work on the MCE is focused on bulk MCMs containing rare earth elements since the entropy change scales with magnetic moment per atom, which is high for rare earth elements.[26,27] But with limited availability and high cost, many efforts are being taken to explore rare earth-free MCMs.[3,28,29] However, the rare earth-based materials exhibit a narrow working temperature span and require a large applied field to acquire reasonable MCE.[24,30] Hence, we have designed a rare earth-free magnetic material system capable of exhibiting the MCE at a relatively broad range of temperatures. The present study is focused on the MCE properties of superparamagnetic Fe nanoparticles embedded in the TiN thin film grown on a *c*-plane aluminum oxide substrate using pulsed laser deposition. The nanoparticle-surrounding thin film matrix pattern is depicted schematically in Fig. 1. The TiN thin film matrix was chosen as a spacer layer since it is non-magnetic, highly corrosion resistive and can serve as an excellent conduit for extracting heat due to its high thermal conductivity (11 W/mK).[31] This paper reports the isothermal entropy change behaviors of the superparamagnetic Fe nanoparticles above their blocking transitions. Additionally, the refrigerant capacity (RC) results for Fe–TiN nanostructures suggest that a broader range of cooling can be achieved up to room temperature with further optimization of Fe particle size and spacer layer thickness. In its present form, Fe nanoparticles in a TiN matrix are not yet a competitive candidate material for magnetocaloric refrigeration applications. That said, the work presented here is a contribution to a path to find such a material. It shows that by nano-structuring, one can systematically utilize the structure-property relationship in materials science and, at the same time, solve multiple issues which plague some of today's magnetocaloric materials. Those include isothermal entropy change in a relatively small temperature region, insufficient thermal conductivity, and dependence on high cost and potentially toxic materials. Table I summarizes the magnetocaloric parameters of Fe–TiN heterostructured materials and several other transition metal magnetocaloric materials. It should be noted that typical giant-magnetocaloric materials exhibit ΔS of about 25 $Jkg^{-1}K^{-1}$ for ΔB = 3 T.

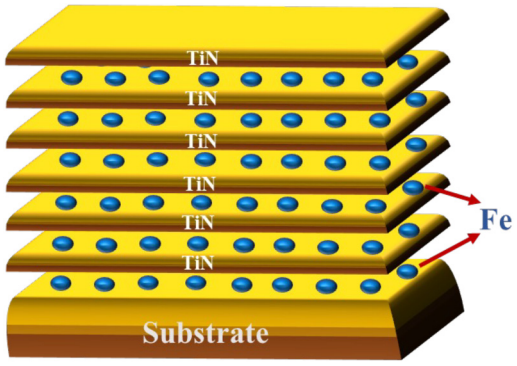

FIG. 1. Schematic of Fe nanoparticle inclusion in TiN thin film matrix in a bilayer configuration represented as Fe–TiN. The dimensions of the substrate, TiN film, and Fe nanoparticles are not to the scale.

II. EXPERIMENTAL DETAILS

Fe particles were deposited in sequential intervals of TiN at 500 °C on *c*-Al_2O_3 substrates. A multi-target pulsed laser deposition system was used for ablating high purity (99.99%) Fe and TiN targets alternately. The experiments were carried out in a high vacuum environment of up to $\sim 5 \times 10^{-7}$ Torr using a Krypton Fluoride (KrF) excimer laser (Lambda Physik) with a radiation wavelength of 248 nm and 30 ns pulse duration. The total thickness of the Fe–TiN sample was fixed by setting 800 pulses for the TiN and 150 pulses for the Fe layer in each period. The laser was operated at a pulse rate of 10 Hz with an energy of 750 mJ, and a target–substrate distance of ∼5 cm was maintained to ensure the uniform deposition of the film. X-ray diffractometer (AXS D8 discover series) with a Bruker monochromatic Cu Kα radiation was used to investigate the structural property of the sample using θ–2θ scan. A cross-sectional electron-transparent sample was prepared using a FEI Helios NanoLab 660 DualBeam for transmission electron microscopy (TEM), scanning TEM (S/TEM) imaging, and energy dispersive x-ray (EDX) spectroscopy elemental mapping. Initially, a 3 μm-thick Pt protective layer was deposited on the selected region to avoid Ga^+ ion beam damage during the lift-out procedure. The final thickness of the lamellae was measured to be around 70 nm. Transmission electron microscopy (TEM) and scanning TEM (STEM) measurements with EDX analysis were performed using a FEI Tecnai Osiris S/TEM, Thermofisher Scientific Inc., operating at 200 kV. TEM image analysis was performed using ImageJ software.[32]

The magnetic properties of Fe–TiN systems were investigated using Vibrating Sample Magnetometer (VSM) attached to a Physical Property Measurement System (PPMS). Magnetization vs field (M vs H) curves were recorded for in-plane fields. Magnetization vs temperature (M vs T) measurements were carried out in different fields. All the magnetization values were calculated by normalizing the moment with respect to the total volume of iron nanoparticles. The total volume of Fe nanoparticles was calculated by multiplying the volume of one nanoparticle by the total number of Fe nanoparticles in the six layers of the sample. The total number of Fe particles in six layers is approximately 1.5×10^{12}. Now, multiplying this total number of particles count with the volume of a single particle $[=(4/3)\pi(d/2)^3]$, where d = 5.0 nm (the average diameter of a nanoparticle), we get the total volume of iron nanoparticles to be 1.01×10^{-7} m^3. The volume of the TiN matrix in six layers is $\sim 9 \times 10^{-7}$ cm^3. The collective contribution of substrate and TiN was subtracted from the Fe–TiN heterostructures by separately recording the magnetization of the sapphire substrate coated with the same thickness of TiN films with no Fe nanoparticles. The sample's surface dimension for the in-plane M vs H and M vs T measurements was 3×5 mm^2.

III. RESULTS AND DISCUSSION

The 2θ XRD diffraction pattern recorded from the Fe–TiN multilayer sample grown on single-crystal *c*-Al_2O_3 substrates is

TABLE I. Magnetocaloric parameters of commonly studied rare earth-free magnetocaloric materials. The magnetocaloric parameters for Fe–TiN nanostructured materials, studied in this work and for bulk Gd are also listed for comparison purpose.

Sample	Sample form	$\|\Delta S\|$ (J/kg K)	$\Delta\mu_0 H$ (T)	RCP (J/kg)	Temperature (K)	Reference
FeNiCr	NP	1.5	5	550	400	52
Gd_5Si_4	NP	3	3	340	320	53
La $(Fe_xSi_{1-x})_{13}$	Bulk	14	2	…	208	54
$MnFeP_{0.5}Si_{0.5}$	Bulk	7	2	173	320	55
γ-Fe_2O_3	NP	1.43	1	163	208	56
Gd	Bulk (single crystal)	5	2	110	293	57
Fe–TiN	NP	0.53	3	94	300	This work
$ZnFe_2O_4$	NP	0.15	1	50	135	58
Co: $Ni_{67}Cu_{33}$	Nanocluster	0.72	7	…	240	59
Fe: $Ni_{61}Cu_{39}$	Nanocluster	0.30	7	…	180	21
$CoFe_2O_4$	NP	0.23	1.3	…	213	60
Co/Au	NP	0.7	1	4.49	9	61
Fe/Cu	Thin film	0.05	1	0.45	50	62

shown in Fig. 2(a). The appearance of only (hkl) planes with (h = k = l = 1 or 2) suggests that the TiN film matrix is textured with respect to (111) planes. The lattice constant of TiN film was found to be 0.421 nm, which was the average calculated from the (111) and (222) d-values in the expression: $\frac{1}{d^2} = \frac{h^2+k^2+l^2}{a^2}$.[33] There are no visible peaks corresponding to Fe particles embedded in the TiN film matrix. The absence of Fe peaks may be because of their low volume fraction (~11%) that is calculated by dividing the volume of Fe particles (1.01×10^{-7} m^3) by the volume of TiN thin film matrix (9.0×10^{-7} cm^3) and small size of Fe particles in the TiN thin film matrix.[34–37] However, the presence of Fe particles embedded in the TiN thin film matrix is confirmed by the TEM and STEM images [Figs. 2(b) and 2(d)] as discussed in this section.

The thickness of TiN layers varies slightly and is highest for the layer that is near the sapphire substrate and lowest for the layer that is farthest from the substrate. The thickness of the bottom-most TiN layer is ~10.6 nm, while the thickness of the topmost TiN layer is 7.0 nm. The difference in the TiN layer thickness is believed to be due to the effect of the substrate on film growth. The average thickness was 8.8 nm, which was used in the calculation of TiN volume and, subsequently, the volume fraction of Fe particles (~5 nm). The lattice constant of TiN calculated from HRTEM images (0.416 nm) is very close to that calculated from XRD (0.421 nm). Similarly, the lattice constant of α-Fe calculated from the HRTEM (110) lattice fringes was 0.283 nm, which is very close to the theoretical value of 0.286 nm. The corresponding Fast Fourier Transform (FFT) [the inset of Fig. 2(b)] reflects the poly-crystalline nature of the TiN material. While TiN reflections were readily identified, it was difficult to identify reflections associated with Fe due to its relatively low volume fraction.

The HAADF image displays the atomic number contrast between Fe particles and TiN [Fig. 2(c)], and corresponding STEM EDX maps [Fig. 2(d)] clearly show the presence of alternating layers of Fe and TiN. To determine the total number of Fe nano-particles, we have multiplied the number of Fe particles observed in the STEM image in one layer by the total number of Fe-layers (=6). A clear delineation of Fe particles in the HRTEM image is difficult since the sample is relatively thick compared to the diameter of an Fe nanoparticle, and thus, the image is formed through a number of Fe nanoparticles that are not aligned.

The M–H hysteresis loops obtained at various temperatures are depicted in Fig. 3(a). The coercivity, extracted from the M–H graph, is plotted against temperature in the inset of Fig. 3(a). It is apparent from the inset that the coercivity decrease with increasing temperature.[38] As the temperature increases, the spins' thermal energy (k_BT) increases that enables them to cross the energy barrier (ΔE) for the spin-reversal, $\Delta E = KV_{np}$, where K is the magnetocrystalline anisotropy constant and V_{np} is the volume of an individual nanoparticle. When the spin-reversal time is faster than the Néel relaxation time, coercivity disappears, and the nanoparticles are said to be in the superparamagnetic state. In the superparamagnetic state, an external magnetic field is able to align the magnetized nanoparticles like superspins. This remains valid as long as the exchange interaction of spins within a nanoparticle makes them to be basically one big magnetic moment. Beyond a certain temperature, the magnetic order of the single domain particles breaks down and the system behaves like a regular paramagnet of individual atomic spins. Normally, any ferromagnetic or ferrimagnetic material undergoes a transition to a paramagnetic state above its Curie temperature. Superparamagnetism is different from this phase transition because it is a dynamic non-equilibrium phenomenon, which occurs below the Curie temperature of the material. In Fig. 3(b), the sample's magnetization (M) is plotted against the applied field normalized with respect to temperature (H/T). The collapse of M–H/T plots to one another is the signature of the nanoparticles' existence in the superparamagnetic state as per the Langevin function $m = L(\mu B/k_BT)$.[39–41] It is clear from the plots in Fig. 3(b) that the sample shows superparamagnetic behavior above 50 K. As the temperature goes down below T_B, the energy barriers between up-and-down spin states are too high ($k_BT \ll KV$) to be overcome by the thermal energy on the time scale of the magnetic measurements. As a result, coercivity increases below 50 K.

Different studies have indicated that magnetic hysteresis and thermal hysteresis may lead to spurious positive isothermal entropy

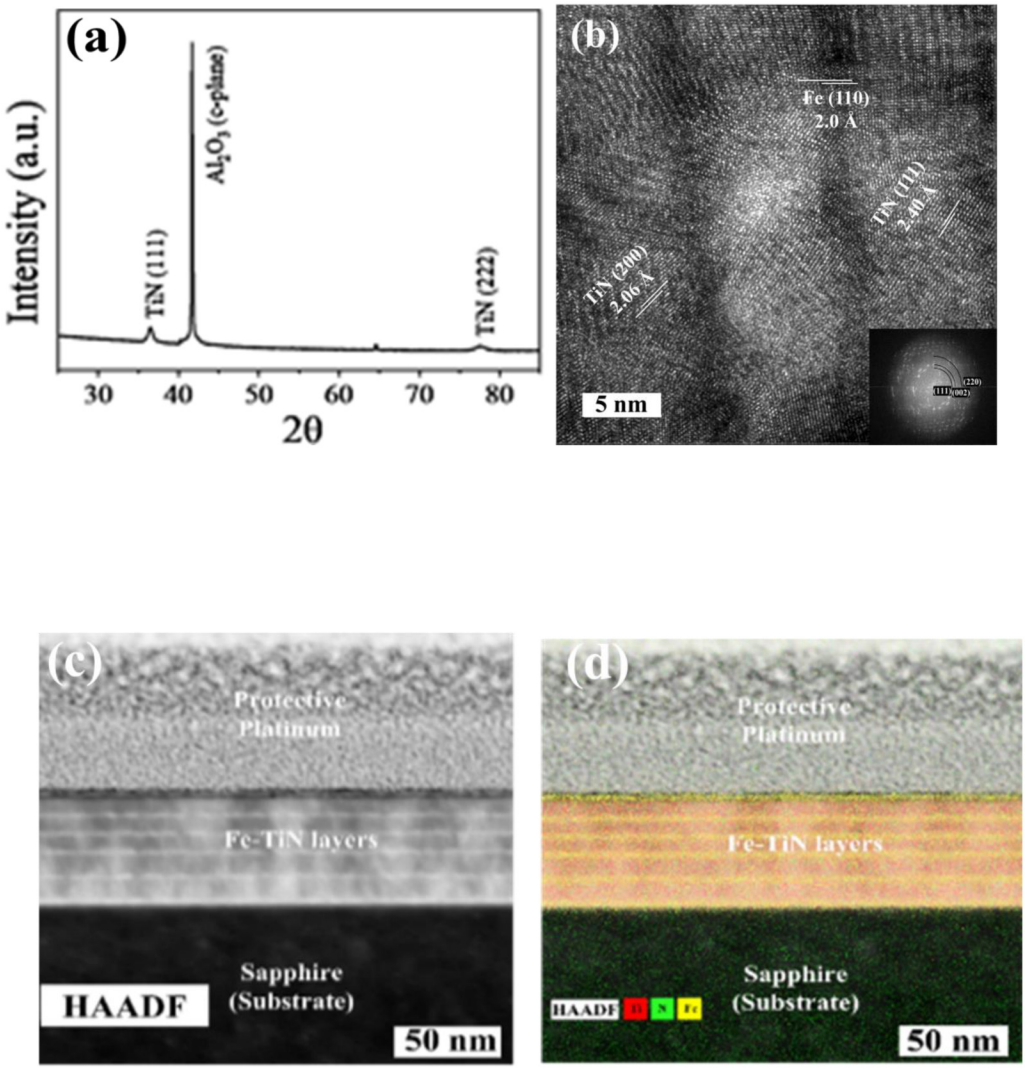

FIG. 2. (a) X-ray diffraction pattern of Fe–TiN multilayer sample grown on a c-Al_2O_3 substrate at 500 °C. (b) HRTEM image of the same sample showing the inclusion of Fe nanoparticles in the TiN thin film matrix. The corresponding FFT pattern (inset) corroborates the TiN polycrystallinity. Lattice spacings are noted on the image for different planes of TiN and Fe. (c) High angle annular dark-field (HAADF) image and (d) elemental map showing the alternating layers of Fe and TiN.

changes that are not necessarily a magnetocaloric effect usable in thermodynamic cycles.[42,43] To study the effect of thermal hysteresis, we have carried out M–T measurements in three different modes. In the zero-field cooling (ZFC) mode, the sample was cooled from T = 300 K above the blocking temperature down to 10 K with no external field applied. After reaching 10 K, an external magnetic field (0.025, 0.05, 0.1, and 0.5 T) was applied, and magnetization was recorded by heating to 300 K at an interval of 10 K. We took magnetization data on cooling the sample from 300 to 10 K in the presence of various constant applied magnetic field in the field cooling (FC) mode. In order to show that FC brings the system to a state of thermal equilibrium, we also measured the magnetization after FC on subsequent field heating (FH) from 10 to 300 K. The absence of thermal hysteresis is evidence that the system is in a state of thermal equilibrium during FC and FH. Shown in Fig. 4 are the results of those experiments where M vs T are plotted for four magnetic fields of 0.025, 0.05, 0.1, and 0.5 T. As seen in this figure, there is no separation between FC and subsequent FH curves, but there is a pronounced bifurcation between ZFC and FH curves at all fields. The bifurcation temperature point between ZFC and FH curves or the peak temperature of ZFC curves is known as the blocking temperature. From Fig. 4 one can also observe that, with increasing magnetic field strength, the bifurcation point becomes undetectable. This is expected because, in

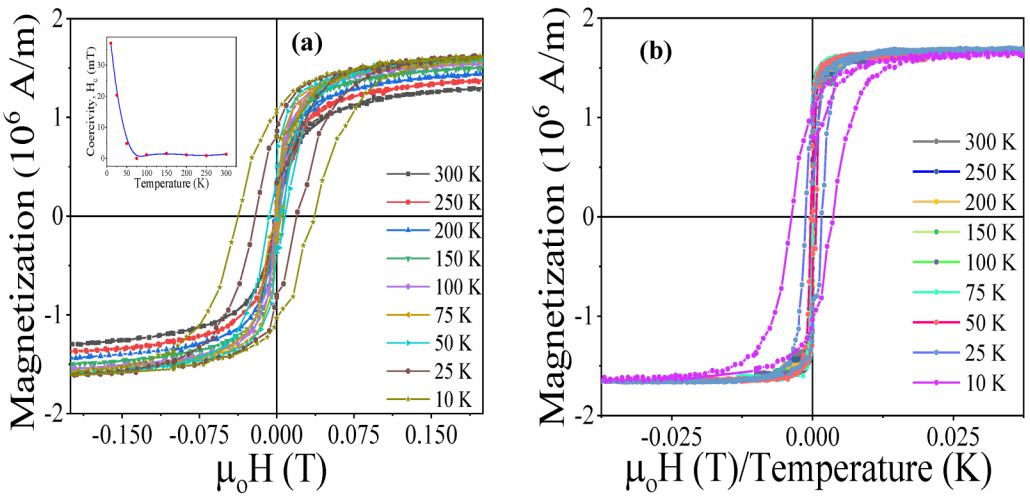

FIG. 3. (a) Magnetic field dependence of magnetization M(H) data at various temperatures from 10 to 300 K for Fe–TiN multilayer sample. The inset of (a) shows the variation of coercivity with temperature. (b) Magnetization plotted against applied field (H) over temperature (K).

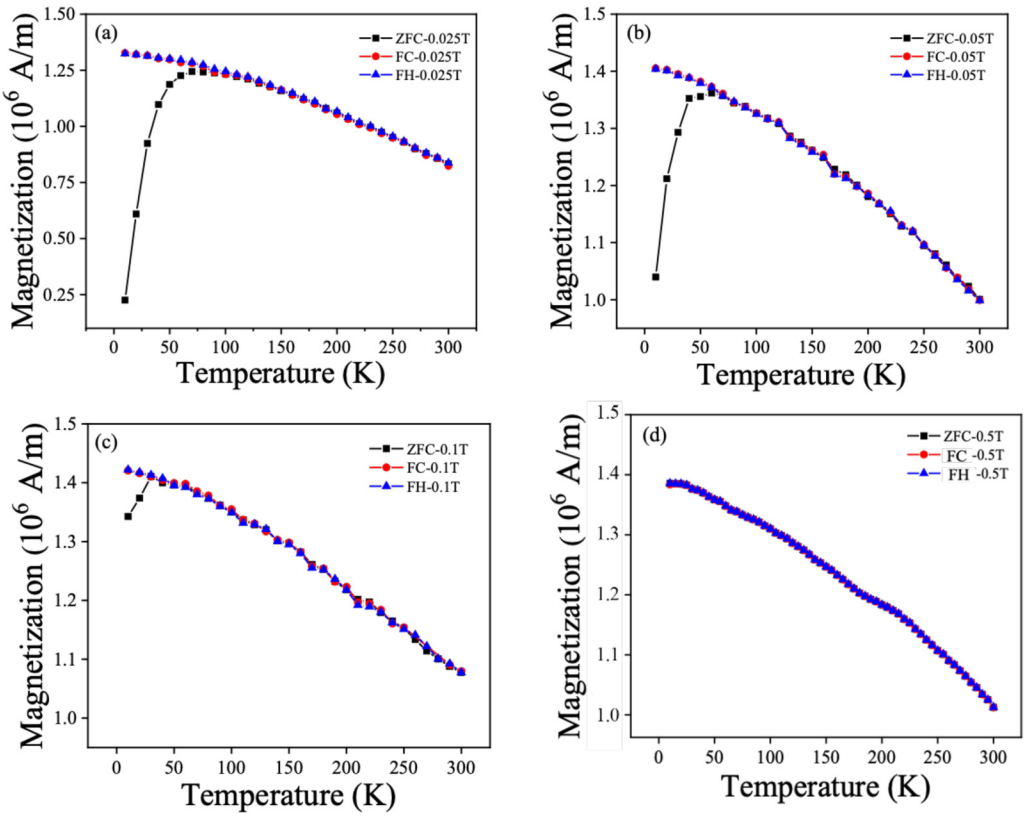

FIG. 4. Zero-field cooled (ZFC) magnetization, field cooled (FC) cooling, and field cooled warming (FH) magnetization as a function of temperature at a field range of (a) 0.025, (b) 0.05, (c) 0.1, and (d) 0.5 T for Fe–TiN multilayer.

very large magnetic fields, the Zeeman energy is large enough to align blocked nanoparticles. In the limit of very large magnetic fields where the Zeeman energy overcomes the anisotropy energy, there is no splitting and, hence, this method fails to detect the blocking temperature.

If the sample is cooled in zero field, the system is blocked in a state which is in an equilibrium state for H = 0, but the system is in a non-equilibrium state when the sample is exposed to a magnetic field after ZFC below the blocking temperature. On the other hand, FC in the presence of an applied magnetic field from above to below the blocking temperature is an equilibrium process as evidenced by the absence of thermal hysteresis between FC and subsequent FH. The isothermal entropy change was measured using an indirect method. In the indirect method (used in the present study), the sample's magnetization is measured as a function of temperature at various external field strengths. Applying Maxwell's relation, the slopes of the M–T curves are used to obtain the magnetic field-induced isothermal entropy change, which is then used to characterize the refrigerant capacity of the magnetic materials. The use of a Maxwell relation to determine the isothermal entropy change is less straight-forward below the blocking temperature, T_B, where M vs H develops dynamic hysteresis and M vs T differs, e.g., for field cooling and zero–field cooling field protocols. The presence of hysteresis originates from the presence of long-lived metastable non-equilibrium states which correspond to relative minima in the Gibbs free energy. The Maxwell relation is a rigorous result of equilibrium thermodynamics and, as such, can only be applied when the system is in a state of thermal equilibrium. However, the presence of magnetization hysteresis at $T < T_B$ does not exclude equilibrium paths in the M–T–H state space. For instance, when cooling the superparamagnetic sample from $T > T_B$ to below T_B in the presence of an applied H-field, its magnetization $M(T, H = \text{const})$ is the equilibrium magnetization for all temperatures, because along the path $(T > T_B,\ H = \text{const}) \rightarrow (T < T_B,\ H = \text{const})$, the system stays in the absolute minimum of the Gibbs free energy. Hence, for $M(T,H)$ data obtained via field cooling protocols, the Maxwell relation is applicable. We used this insight to analyze the isothermal entropy change for $T < T_B$. Although the analysis of isothermal entropy change is meaningful for $T < T_B$, hysteretic paths in M–T–H space associated with a refrigeration cycle render the regime at $T < T_B$ unfit for applications. For $T > T_B$, the Fe nanoparticles embedded in TiN thin film matrix behave superparamagnetic and are free of any hysteresis above the blocking temperature. The change in entropy while changing the magnetic field is explained using the classical theory of thermodynamics as

$$\Delta S\,(T,\ H) = S(T,\ H_f) - S(T,\ H_i) = \int_{H_i}^{H_f} \left(\frac{\partial S}{\partial H}\right)_T dH. \quad (1)$$

By using Maxwell's relation,

$$\left(\frac{\partial S(T,\ H)}{\partial H}\right)_T = \mu o V \left(\frac{\partial M(T,\ H)}{\partial T}\right)_H. \quad (2)$$

Substituting Eq. (2) into Eq. (1) yields

$$\Delta S\,(T,\ H) = \mu o V \int_{H_i}^{H_f} \left(\frac{\partial M(T,\ H)}{\partial T}\right)_H dH, \quad (3)$$

where μ_o is the vacuum permeability, V is the volume of the material, H_i and H_f represent the initial (typically zero) and final applied magnetic fields, and ΔS is the magnetic field-induced isothermal entropy change. The FC M–T curves plotted in Fig. 4 were differentiated to obtain the change in magnetization with respect to temperature, as shown in Fig. 5. The negative values of ΔS of 137, 95, and 47 J/Km^3 are noted for 300 K at 0.075, 0.05, and 0.025 T, respectively [Fig. 5(a)]. We have also carried out MCE studies at higher applied fields (0.1–3 T) as shown in Fig. 5(b). The ΔS vs T profiles show a nearly flat behavior up to room temperature. For example, the negative values of ΔS (normal or forward MCE) at 3 T are 1.9×10^3, 2×10^3, 2.4×10^3, and 4.18×10^3 J/K m^3 at 50, 100, 200, and 300 K, respectively, indicating a relatively weak temperature dependence with respect to the ΔS drop in ferromagnetic

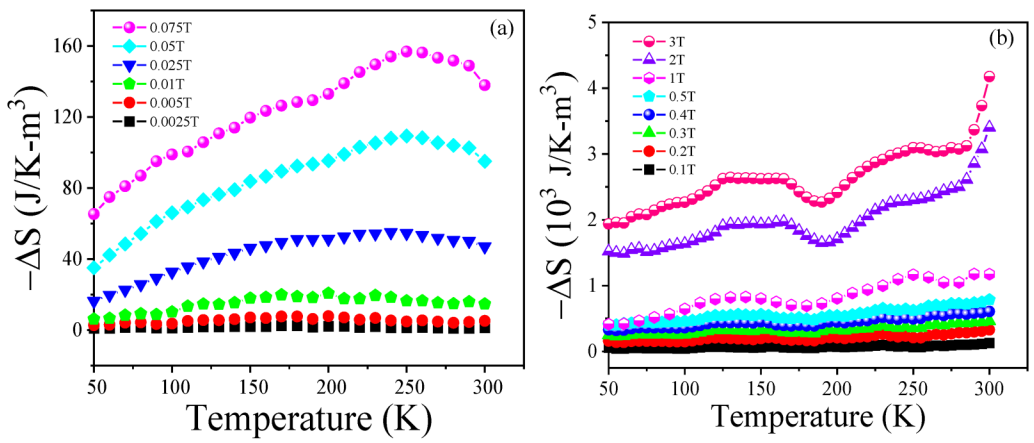

FIG. 5. Temperature dependence of the magnetic entropy change ΔS obtained under (a) low fields (2.50–75 mT and (b) high fields (0.1–3 T).

materials.[44] Thus, it is clear from these data that a reasonably high ΔS could be maintained in the Fe–TiN system well above the Fe nanoparticles blocking temperature.

It can be noted from Fig. 5(b) that the non-uniform variation in ΔS is almost absent up to 1 T and becomes very pronounced at 3 T, a field strength that should be avoided in applications. For moderate applied magnetic fields, as envisioned in refrigeration applications, the non-uniformity is not significant. We believe that this non-uniform variation in ΔS is related to the particle size distribution in the following manner. As long as the Fe nanoparticle is magnetically ordered and acts as a superparamagnetic particle, the magnitude of its isothermal entropy change can only decrease with increasing temperature (see quantitative discussion below). Clearly, no functional form of a particle distribution can explain the opposite effect. A fraction of the particles is believed to be small enough that finite size effects arise for the Fe particles. These finite size effects significantly reduce the Curie temperature of the particles bringing them close to room temperature. A similar effect has been observed by some of the authors in very thin layers of Co films designed for MC effects.[23] When the temperature approaches the Curie temperature of this subset of very small particles, entropy change from the second order phase transition between ferromagnetic order and paramagnetism is activated and contributes the entropy change. We believe this is why this anomaly is present at the high-temperature end of our entropy data. The total magnetic moment of the Fe nanoparticles can be approximated by

$$m = \sum_i N_i m_{0,i} \tanh\left(\frac{m_{0,i}B}{k_b T}\right), \tag{4}$$

where N_i is the number of particles with saturation moment $m_{0,i}$ and $B = \mu_0 H$. The temperature dependence is for simplicity approximated by an Ising model which is a crude approximation for particles with large anisotropy. The argument could be generalized for other Brillouin functions. The isothermal entropy change of such an ensemble of particles can be expressed as

$$\Delta S = -\sum_i N_i \left(k_B \ln \cosh \frac{Bm_{0,i}}{k_B T} - Bm_{0,i} \tanh\left(\frac{Bm_{0,i}}{k_B T}\right)\right). \tag{5}$$

Each term in this sum has a low-temperature limit given by a constant value $\Delta S_i = -k_B N_i \ln 2$ and a high-temperature limit of $\Delta S_i = 0$ with an inflection point whose temperature position is determined by $m_{0,i}B$ and shifts to higher temperatures with increasing $m_{0,i}B$. In this way, by summing up contributions with inflection points at ever higher temperatures, one reaches a region with little to no temperature dependence. As noted in ZFC/FH M-T curves, the ZFC–FH bifurcation temperature and the peak temperature of ZFC are close to each other but are not identical, indicating a narrow particle size distribution. For example, the ZFC peak temperature is 50 K while the ZFC–FH bifurcation temperature is 57 K at 50 mT, whereas the ZFC peak temperature and the ZFC–FH bifurcation temperature are nearly identical (~30 K) at 100 mT. The Fe–TiN system has also exhibited an absence of thermal hysteresis that is evident from a superimposition of the field cooled cooling (FC) and field cooled warming (FH) M–T curves (Fig. 4). These trends improve the operation of cooling devices and mitigate the narrow working temperature span of MCMs. The ΔS has a weak temperature dependence that brings about a wide working temperature range and large refrigerant capacity. This ΔS has an upper limit (total area under the curve) and must follow the area sum rule, which is given by the following expression:[45,46]

$$\int_0^\infty |s(T, H)| dT = {}_o M_s H. \tag{6}$$

In this equation, s (= ΔS/V) term has been introduced to keep the dimensional computability on both sides of the equation. The sum rule implies that among the two materials with the same saturation magnetization M_S, the material with a larger entropy difference between an adiabatically magnetized state and an adiabatically

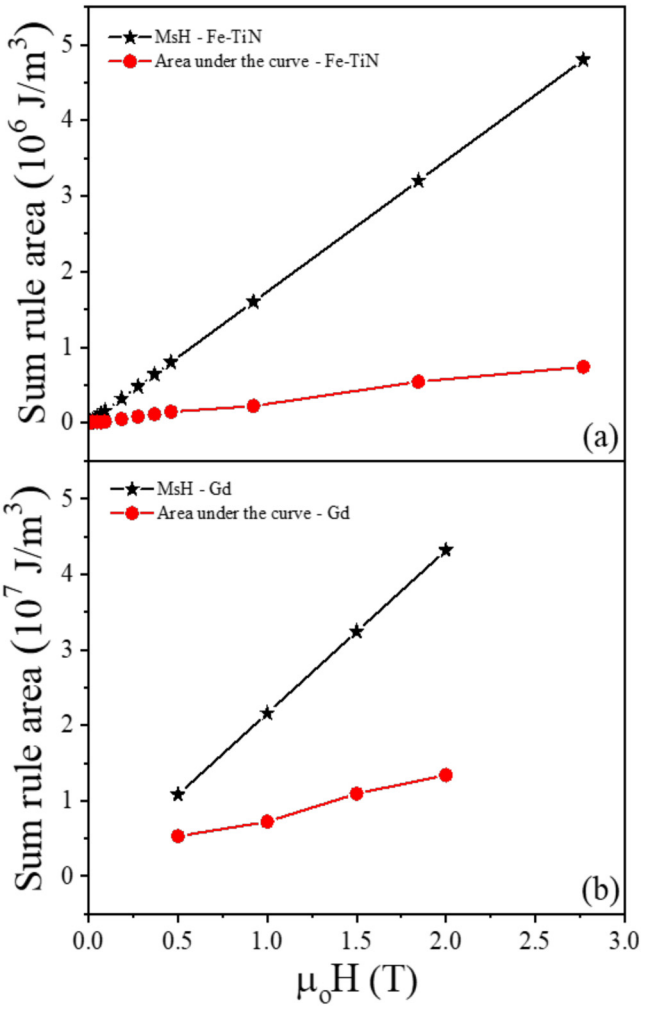

FIG. 6. Sum rule area as a function of applied magnetic fields for (a) Fe–TiN heterostructure and (b) bulk gadolinium.

demagnetized state at a given temperature may have low entropy change at other temperatures. The sum rule also implies that a material that does not have a large entropy change at any temperature may undergo a moderate entropy change over a broader temperature.[47,48] In addition, the sum rule also serves as a useful tool to cross-check the numerical analysis of the data. If the area is larger than the theoretically possible limit, μoM_sH, a flaw in the numerical analysis is easily revealed. Ferromagnetic magnetocaloric materials with high Curie temperatures have already been used[49,50] for higher operating temperatures. But even with a large magnetic moment, the working temperature range for the magnetic phase change remains modest. The significance of the area sum rule comes from the fact that the Fe–TiN heterostructure shows a wide working temperature range while satisfying the theoretical validation. The red line in Fig. 6(a) shows the total values of the area under the curve obtained by numerical integration of the ΔS vs T experimental curves at higher fields presented in Fig. 5(b). The wide working temperature can be used in devices where cooling is required over a broad temperature range. The area sum rule is satisfied for all the applied fields as the M_sH (the maximum ΔS obtainable by having independent atomic spins in the immediate vicinity of Curie point) values depicted by the black line are greater than the areas obtained by numerical integration of the experimental curves. Using the ΔS vs T data of Ref. 51, we have generated a figure [Fig. 6(b)] for bulk Gd that is similar to our Fig. 6(a). Though the sum rule area of Gd is one order of magnitude larger than our Fe–TiN samples, the nature of M_sH vs $\Delta S \times T$ area curves for Gd and Fe–TiN samples are similar. Using the numbers in Fig. 6, the theoretical cooling efficiency [$\eta=(M_sH - \Delta ST/M_sH)$] was found to be 77% and 83% at 2 T for bulk Gd and nanostructured Fe–TiN system, respectively. Thus, at 2 T, Gd is 23% away of the theoretical cooling limit while our nanoparticles are 17% away from the theoretical limit. The refrigerant capacity (RC) is employed for relatively high ΔS, which can be calculated using the following formula:

$$RC = \int_{T_{min}}^{T_{max}} |\Delta S(T,\ H)|\ dT. \tag{7}$$

Figure 7 shows the field dependence of RC of a Fe–TiN heterostructure. The RC values increase with an increase in the magnetic field; the maximum value is 7.4×10^5 J/m^3 (~94 J/kg) at 3 T. The RC at lower fields 0.025, 0.05, and 0.075 T are found to be 1×10^4, 2.2×10^4, and 3.2×10^3 J/m^3, respectively.

Table I lists the magnetocaloric parameters of Fe–TiN heterostructure and rare earth-free nanostructured transition metal-based magnetocaloric materials commonly reported in the literature. The magnetocaloric parameters for bulk Gd are also listed in this table for comparison purpose.

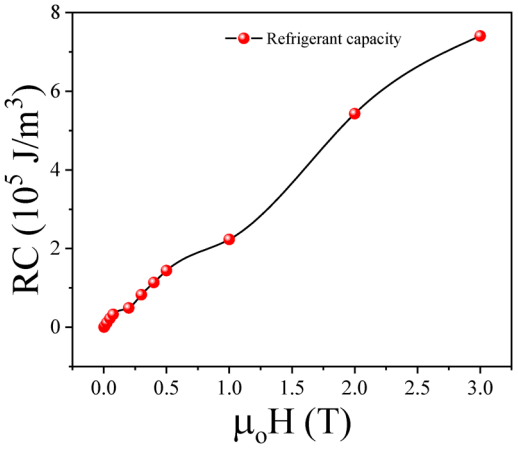

FIG. 7. RC vs field of Fe–TiN heterostructure in the 10–300 K temperature range for the integral in Eq. (7) used to determine RC.

IV. CONCLUSIONS

In summary, we have studied the structural, magnetic, and magnetocaloric properties of Fe nanoparticles embedded in TiN thin film that were grown on a *c*-plane Al_2O_3 substrate using the PLD technique. With the absence of a dynamic magnetic hysteresis above the blocking temperature, the negative ΔS as high as 4.18×10^3 J/Km^3 is obtained at 3 T at 300 K. Although the isothermal entropy change observed in the Fe nanoparticles embedded TiN multilayer is lower by almost an order of magnitude in the existing state-of-the-art magnetocaloric materials, our finding reports observation of the MCE in a single element material system that is along the word-wide efforts to design and develop rare earth-free simple MCMs. The RC at various applied fields have been evaluated with the realization of a maximum of RC values of 7.4×10^5 J/m^3 (~94 J/kg) at 3 T. With a combination of a broad range of usable ΔS and easy accessibility, the Fe–TiN material system can give us insight for the fabrication and design of novel MCMs with improved refrigeration efficiency needed for next-generation solid-state cooling.

ACKNOWLEDGMENTS

This work was carried out with the support from the NSF Partnership for Research and Education in Materials (PREM) grant (DMR-2122067) and forms the part of Ph.D. dissertation of K.S. J.E.S. acknowledge the support of the National Science Foundation (NSF) through the Materials Research Science and Engineering Center (MRSEC) (Grant No. DMR-1420645). The research was performed in part in the Nebraska Nanoscale Facility: National Nanotechnology Coordinated Infrastructure under Award No. ECCS: 2025298 and with support from the Nebraska Research Initiative through the Nebraska Center for Materials and Nanoscience and the Nanoengineering Research Core Facility at the University of Nebraska-Lincoln. This work also made use of the Cornell Center for Materials Research Shared Facilities, which are supported through the NSF MRSEC Program (No. DMR-1719875). Ch.B. acknowledges support by the National Science Foundation through EPSCoR RII Track-1: Emergent Quantum Materials and Technologies (EQUATE), Award OIA-2044049.

AUTHOR DECLARATIONS

Conflict of Interest

The authors have no conflicts to disclose.

Author Contributions

Kaushik Sarkar: Data curation (lead); Formal analysis (lead); Investigation (lead); Software (equal); Visualization (equal); Writing – original draft (equal). **Surabhi Shaji:** Data curation (supporting); Formal analysis (supporting); Writing – review & editing (supporting). **Suchit Sarin:** Investigation (equal); Resources (equal); Validation (equal). **Jeffrey E. Shield:** Resources (equal); Writing – original draft (equal); Writing – review & editing (equal). **Christian Binek:** Conceptualization (equal); Funding acquisition (equal); Validation (equal); Writing – original draft (equal); Writing – review & editing (equal). **Dhananjay Kumar:** Conceptualization (lead); Funding acquisition (equal); Resources (equal); Supervision (equal); Validation (equal); Visualization (lead); Writing – original draft (equal); Writing – review & editing (lead).

DATA AVAILABILITY

The data that support the findings of this study are available from the corresponding author upon reasonable request.

REFERENCES

[1]V. K. Pecharsky and K. A. Gschneidner, Jr., "Magnetocaloric effect and magnetic refrigeration," J. Magn. Magn. Mater. **200**(1–3), 44–56 (1999).
[2]S. Vdovichev, N. Polushkin, I. Rodionov, V. Prudnikov, J. Chang, and A. Fraerman, "High magnetocaloric efficiency of a NiFe/NiCu/CoFe/MnIr multilayer in a small magnetic field," Phys. Rev. B **98**(1), 014428 (2018).
[3]E. Brück, O. Tegus, X. Li, F. De Boer, and K. Buschow, "Magnetic refrigeration—Towards room-temperature applications," Physica B **327**(2–4), 431–437 (2003).
[4]M. S. El Hadri, V. Polewczyk, Y. Xiao, S. Mangin, and E. Fullerton, "Large anisotropic magnetocaloric effect in all-sputtered epitaxial terbium thin films," Phys. Rev. Mater. **4**(12), 124404 (2020).
[5]S. K. Vandrangi, J.-C. Yang, Y.-M. Zhu, Y.-Y. Chin, H.-J. Lin, C.-T. Chen, Q. Zhan, Q. He, Y.-C. Chen, and Y.-H. Chu, "Enhanced magnetocaloric effect driven by interfacial magnetic coupling in self-assembled Mn_3O_4–$La_{0.7}Sr_{0.3}MnO_3$ nanocomposites," ACS Appl. Mater. Interfaces **7**(48), 26504–26511 (2015).
[6]V. Chaudhary, X. Chen, and R. V. Ramanujan, "Iron and manganese based magnetocaloric materials for near room temperature thermal management," Prog. Mater. Sci. **100**, 64–98 (2019).
[7]P. Weiss and A. Piccard, "Sur un nouveau phénomène magnétocalorique," Comptes Rendus **166**, 352–354 (1918).
[8]W. Giauque and D. MacDougall, "The production of temperatures below one degree absolute by adiabatic demagnetization of gadolinium sulfate," J. Am. Chem. Soc. **57**(7), 1175–1185 (1935).
[9]J. R. Gómez, R. F. Garcia, A. D. M. Catoira, and M. R. Gómez, "Magnetocaloric effect: A review of the thermodynamic cycles in magnetic refrigeration," Renew. Sustain. Energy Rev. **17**, 74–82 (2013).
[10]A. Barman, S. Kar-Narayan, and D. Mukherjee, "Caloric effects in perovskite oxides," Adv. Mater. Interfaces **6**(15), 1900291 (2019).
[11]K. A. Gschneidner, Jr., V. Pecharsky, and A. Tsokol, "Recent developments in magnetocaloric materials," Rep. Prog. Phys. **68**(6), 1479 (2005).
[12]L.-W. Li, "Review of magnetic properties and magnetocaloric effect in the intermetallic compounds of rare earth with low boiling point metals," Chin. Phys. B **25**(3), 037502 (2016).
[13]G. Daniel-Pérez, J. L. Sánchez Llamazares, A. Quintana-Nedelcos, P. Álvarez-Alonso, R. Varga, and V. Chernenko, "Magnetostructural transition and magnetocaloric effect in $MnNiGe_{1.05}$ melt-spun ribbons," J. Appl. Phys. **115**(17), 17A920 (2014).
[14]T. V. Jayaraman, M. A. Koten, and J. E. Shield, "Near room temperature magnetocaloric properties of melt-spun $Gd_{100-x}B_x$ (x= 0, 5, 10, 15, and 20 at%) alloys," J. Magn. Magn. Mater. **323**(15), 2037–2041 (2011).
[15]J. Ćwik, Y. Koshkid'ko, N. de Oliveira, K. Nenkov, A. Hackemer, E. Dilmieva, N. Kolchugina, S. Nikitin, and K. Rogacki, "Magnetocaloric effect in Laves-phase rare-earth compounds with the second-order magnetic phase transition: Estimation of the high-field properties," Acta Mater. **133**, 230–239 (2017).
[16]M.-H. Phan and S.-C. Yu, "Review of the magnetocaloric effect in manganite materials," J. Magn. Magn. Mater. **308**(2), 325–340 (2007).
[17]V. V. Khovaylo, V. V. Rodionova, S. N. Shevyrtalov, and V. Novosad, "Magnetocaloric effect in 'reduced' dimensions: Thin films, ribbons, and microwires of Heusler alloys and related compounds," Phys. Status Solidi B **251**(10), 2104–2113 (2014).
[18]S. Hariharan and J. Gass, "Superparamagnetism and magneto-caloric effect (MCE) in functional magnetic nanostructures," Rev. Adv. Mater.Sci. **10**, 398–402 (2005).
[19]P. Lampen, A. Puri, M. Phan, and H. Srikanth, "Structure, magnetic, and magnetocaloric properties of amorphous and crystalline $La_{0.4}Ca_{0.6}MnO_3$ δ nanoparticles," J. Alloys Compd. **512**, 94–99 (2012).
[20]S. Thota, Q. Zhang, F. Guillou, U. Lüders, N. Barrier, W. Prellier, A. Wahl, and P. Padhan, "Anisotropic magnetocaloric effect in all-ferromagnetic ($La_{0.7}Sr_{0.3}MnO_3$/$SrRuO_3$) superlattices," Appl. Phys. Lett. **97**(11), 112506 (2010).
[21]S. Michalski, R. Skomski, T. Mukherjee, X.-Z. Li, C. Binek, and D. J. Sellmyer, "Magnetic entropy changes in nanogranular Fe: $Ni_{61}Cu_{39}$," J. Appl. Phys. **109**(7), 07A936 (2011).
[22]A. Barman, S. Chatterjee, J. K. Dey, A. Datta, and D. Mukherjee, "Interface-induced enhanced magnetocaloric effect in an epitaxial Co Fe_2O_4/$La_{0.7}Sr_{0.3}MnO_3$ heterostructure," Phys. Rev. B **102**(5), 054433 (2020).
[23]T. Mukherjee, S. Sahoo, R. Skomski, D. J. Sellmyer, and C. Binek, "Magnetocaloric properties of Co/Cr superlattices," Phys. Rev. B **79**(14), 144406 (2009).
[24]V. Chaudhary and R. V. Ramanujan, "Magnetocaloric properties of Fe-Ni-Cr nanoparticles for active cooling," Sci. Rep. **6**(1), 35156 (2016).
[25]K. Das and I. Das, "Giant enhancement of magnetocaloric effect at room temperature by the formation of nanoparticle of $La_{0.48}Ca_{0.52}MnO_3$ compound," J. Appl. Phys. **119**(9), 093903 (2016).
[26]L. Li, Y. Yuan, Y. Qi, Q. Wang, and S. Zhou, "Achievement of a table-like magnetocaloric effect in the dual-phase $ErZn_2$/ErZn composite," Mater. Res. Lett. **6**(1), 67–71 (2018).
[27]S. Roy, N. Khan, and P. Mandal, "Giant low-field magnetocaloric effect in single-crystalline $EuTi_{0.85}Nb_{0.15}O_3$," APL Mater. **4**(2), 026102 (2016).
[28]X. Moya, L. Hueso, F. Maccherozzi, A. Tovstolytkin, D. Podyalovskii, C. Ducati, L. Phillips, M. Ghidini, O. Hovorka, and A. Berger, "Giant and reversible extrinsic magnetocaloric effects in $La_{0.7}Ca_{0.3}MnO_3$ films due to strain," Nat. Mater. **12**(1), 52–58 (2013).
[29]S. Shaji, N. R. Mucha, P. Giri, C. Binek, and D. Kumar, "Magnetic and magnetocaloric properties of Fe_2Ta thin films," AIP Adv. **10**(2), 025222 (2020).
[30]B. Yu, Q. Gao, B. Zhang, X. Meng, and Z. Chen, "Review on research of room temperature magnetic refrigeration," Int. J. Refrig. **26**(6), 622–636 (2003).
[31]M. K. Samani, X. Z. Ding, N. Khosravian, B. Amin-Ahmadi, Y. Yi, G. Chen, E. C. Neyts, A. Bogaerts, and B. K. Tay, "Thermal conductivity of titanium nitride/titanium aluminum nitride multilayer coatings deposited by lateral rotating cathode arc," Thin Solid Films **578**, 133–138 (2015).
[32]C. A. Schneider, W. S. Rasband, and K. W. Eliceiri, "NIH image to ImageJ: 25 years of image analysis," Nat. Methods **9**(7), 671–675 (2012).

[33]P. Joshi, A. Haque, S. Gupta, R. J. Narayan, and J. Narayan, "Synthesis of multifunctional microdiamonds on stainless steel substrates by chemical vapor deposition," Carbon **171**, 739–749 (2021).
[34]D. Kumar, J. Narayan, A. Kvit, A. Sharma, and J. Sankar, "High coercivity and superparamagnetic behavior of nanocrystalline iron particles in alumina matrix," J. Magn. Magn. Mater. **232**(3), 161–167 (2001).
[35]D. Kumar, A. Sarin, V. Verma, and R. Venkatraman, "Pulsed laser deposition assisted fabrication and characterization of Fe–Co nanoparticles embedded in TiN thin film matrix," Thin Solid Films **534**, 561–565 (2013).
[36]K. Sarkar, P. Jaipan, J. Choi, T. Haywood, D. Tran, N. R. Mucha, S. Yarmolenko, O. Scott-Emuakpor, M. Sundaresan, R. K. Gupta, and D. Kumar, "Enhancement in corrosion resistance and vibration damping performance in titanium by titanium nitride coating," SN Appl. Sci. **2**, 949 (2020).
[37]M. Roy, N. R. Mucha, R. G. Ponnam, P. Jaipan, O. Scott-Emuakpor, S. Yarmolenko, A. K. Majumdar, and D. Kumar, "Quantum interference effects in titanium nitride films at low temperatures," Thin Solid Films **681**, 1–5 (2019).
[38]S. Shaji, N. R. Mucha, A. K. Majumdar, C. Binek, A. Kebede, and D. Kumar, "Magnetic and electrical properties of Fe90Ta10 thin films," J. Magn. Magn. Mater. **489**, 165446 (2019).
[39]B. P. Bastakoti, J. Bentley, D. McLaurin, S.-i. Yusa, S. Shaji, N. R. Mucha, D. Kumar, and T. Ahamad, "Synthesis of magnetite loaded fluorescence micelles of triblock copolymer," J. Mol. Liq. **305**, 112785 (2020).
[40]S. Shaji, "Electrical, magnetic and magnetocaloric properties of Fe-Ta thin films," Ph.D. diss. (North Carolina Agricultural and Technical State University, 2020).
[41]S. Shaji, N. R. Mucha, S. Fialkova, and D. Kumar, "Morphological data on soft ferromagnetic $Fe_{90}Ta_{10}$ thin films," Data Brief **27**, 104714 (2019).
[42]O. Kubo, T. Ido, H. Yokoyama, and Y. Koike, "Particle size effects on magnetic properties of $BaFe_{12-2x}Ti_xCo_xO_{19}$ fine particles," J. Appl. Phys. **57**(8), 4280–4282 (1985).
[43]F. Guillou, H. Yibole, G. Porcari, L. Zhang, N. Van Dijk, and E. Brück, "Magnetocaloric effect, cyclability and coefficient of refrigerant performance in the MnFe (P, Si, B) system," J. Appl. Phys. **116**(6), 063903 (2014).
[44]P. Poddar, J. Gass, D. Rebar, S. Srinath, H. Srikanth, S. Morrison, and E. Carpenter, "Magnetocaloric effect in ferrite nanoparticles," J. Magn. Magn. Mater. **307**(2), 227–231 (2006).
[45]T. Mukherjee, S. Michalski, R. Skomski, D. J. Sellmyer, and C. Binek, "Overcoming the spin-multiplicity limit of entropy by means of lattice degrees of freedom: A minimal model," Phys. Rev. B **83**(21), 214413 (2011).
[46]S. Gama, A. A. Coelho, A. de Campos, A. M. G. Carvalho, F. C. Gandra, P. J. von Ranke, and N. A. de Oliveira, "Pressure-induced colossal magnetocaloric effect in MnAs," Phys. Rev. Lett. **93**(23), 237202 (2004).
[47]R. McMichael, R. Shull, L. Swartzendruber, L. Bennett, and R. Watson, "Magnetocaloric effect in superparamagnets," J. Magn. Magn. Mater. **111**(1–2), 29–33 (1992).
[48]R. Shull, R. McMichael, and J. Ritter, "Magnetic nanocomposites for magnetic refrigeration," Nanostruct. Mater. **2**(2), 205–211 (1993).
[49]B. Shen, J. Sun, F. Hu, H. Zhang, and Z. Cheng, "Recent progress in exploring magnetocaloric materials," Adv. Mater. **21**(45), 4545–4564 (2009).
[50]M. Yue, M. Xu, H. Zhang, D. Zhang, D. Liu, and Z. Altounian, "Structural and magnetocaloric properties of $MnFeP_{1-x}Si_x$ compounds prepared by spark plasma sintering," IEEE Trans. Magn. **51**(11), 1–4 (2015).
[51]R. Essajai, N. Ennassiri, M. Balli, M. Zidane, E. Salmani, O. Mounkachi, M. Rouchdi, A. Abbassi, H. Ez-Zahraouy, A. Mzerd, and N. Hassanain, "Revisiting the magnetic and magnetocaloric properties of bulk gadolinium: A combined DFT and Monte Carlo simulations," Phys. Scr. **96**(1), 015808 (2021).
[52]V. Chaudhary and R. Ramanujan, "Magnetocaloric properties of Fe-Ni-Cr nanoparticles for active cooling," Sci. Rep. **6**(1), 1–9 (2016).
[53]S. Harstad, A. El-Gendy, S. Gupta, V. K. Pecharsky, and R. Hadimani, "Magnetocaloric effect of micro-and nanoparticles of Gd_5Si_4," J. Mater. **71**(9), 3159–3163 (2019).
[54]F.-x. Hu, B.-g. Shen, J.-r. Sun, Z.-h. Cheng, G.-h. Rao, and X.-x. Zhang, "Influence of negative lattice expansion and metamagnetic transition on magnetic entropy change in the compound $LaFe_{11.4}Si_{1.6}$," Appl. Phys. Lett. **78**(23), 3675–3677 (2001).
[55]K. Katagiri, K. Nakamura, and H. Wada, "Magnetocaloric properties and magnetic refrigerant capacity of $MnFeP_{1-x}Si_x$," J. Alloys Compd. **553**, 286–290 (2013).
[56]A. Elouafi, R. Moubah, S. Derkaoui, A. Tizliouine, R. Cherkaoui, S. Shi, A. Bendani, M. Sajieddine, and H. Lassri, "Finite size effects on the magnetocaloric properties around blocking temperature in γ-Fe_2O_3 nanoparticles," Physica A **523**, 260–267 (2019).
[57]K. Gschneidner, Jr. and V. K. Pecharsky, "Magnetocaloric materials," Annu. Rev. Mater. Sci. **30**(1), 387–429 (2000).
[58]P. Thandapani, M. Ramalinga Viswanathan, and J. C. Denardin, "Magnetocaloric effect and universal curve behavior in superparamagnetic zinc ferrite nanoparticles synthesized via microwave assisted Co-precipitation method," Phys. Status Solidi A **215**(11), 1700842 (2018).
[59]S. Michalski, R. Skomski, X.-Z. Li, D. Le Roy, T. Mukherjee, C. Binek, and D. J. Sellmyer, "Isothermal entropy changes in nanocomposite Co: $Ni_{67}Cu_{33}$," J. Appl. Phys. **111**(7), 07A930 (2012).
[60]E. V. Gopalan, I. Al-Omari, D. S. Kumar, Y. Yoshida, P. Joy, and M. Anantharaman, "Inverse magnetocaloric effect in sol–gel derived nanosized cobalt ferrite," Appl. Phys. A **99**(2), 497–503 (2010).
[61]A. Zeleňáková, P. Hrubovčák, V. Zeleňák, J. Kováč, and V. Franco, "Magnetocaloric effect and scaling analysis in superspinglass cobalt based nanoparticles," J. Alloys Compd. **805**, 767–773 (2019).
[62]R. Desautels, C. Shueh, K.-W. Lin, J. Freeland, and J. van Lierop, "Dynamical freezing, magnetic ordering, and the magnetocaloric effect in nanostructured Fe/Cu thin films," Appl. Phys. Lett. **108**(17), 172410 (2016).